De-wrinkling of pre-tensioned membranes

CrossMark

A.S. Bonin, K.A. Seffen *

Department of Engineering, University of Cambridge, Trumpington Street, Cambridge CB2 1PZ, United Kingdom

ABSTRACT

Thin membranes are used in the spacecraft industry as extremely lightweight structural components. They need to be stiffened, usually by applying discrete forces, and this increases their susceptibility to wrinkling in regions where high tensile stresses develop. We consider a regular polygonal membrane uniformly loaded at its corners by equal forces and we prevent wrinkle formation by trimming the edges of the polygon into very gentle curves. We confirm this performance through simple physical experiments using Kapton, a typical membrane material and, using computational analysis, we show how the distribution of compressive stresses, responsible for causing wrinkles, dissipates following trimming. Finally, we accurately predict the required level of trimming for any number of sides of polygon using a simple, linear model, which invokes a plate-bending analogy.

© 2014 The Authors. Published by Elsevier Ltd. This is an open access article under the CC BY license (http://creativecommons.org/licenses/by/3.0/).

1. Introduction

Gossamer structures are thin-walled membranes, or meshes, favoured in the design, construction and operation of lightweight spacecraft, such as solar-propelled sails, optical antennae for space telescopes and, more recently, de-orbiting chutes. Once folded inside restricted payload volumes, they offer the highest packaging ratios of any deployable structure; and post-deployment, the mass-to-area, or "areal", density is much lower than conventional monolithic structures (Santer and Seffen, 2009). Correspondingly, they afford greater potential for launching sails and telescopes of ever increasing size, but after deployment the membrane must be stiffened to be effective in operation. Current design architectures centre on polygonal layouts pre-tensioned by means of cables attached to their vertices, and shown schematically in Fig. 1(a). The membrane is largely unobstructed for maximal reflection of incident light or radio waves, and the cables are connected to a supporting edge structure in this case, which enables pre-tensioning either passively by geometrical means or actively by embedded actuators. The edge structure is not our concern here, but we assume that it functions ideally, by enabling deployment and membranal tensioning without its own members buckling or failing; rather, we focus on the shape of membrane after tensioning, and the potential for *wrinkling*.

In this sense, out-of-plane displacements become important, and the membrane is locally no longer flat, which can disrupt the

reflection quality. If any of the in-plane stresses are compressive, the possibility of out-of-plane buckling increases and, because the membrane is very thin, the buckles have a short wavelength, manifesting as narrow wrinkles. This effect is more pronounced when the loading is applied as discrete forces on the membrane vertices, which concentrate the stress field: high tensile stresses radiate away from the vertex, with a similarly high, orthogonal compression due to the Poisson effect and inevitable wrinkling for all types of loading. Further afield, all of the loads exert an influence so the membrane is locally tensioned in all directions, giving biaxial, sometimes equal, stresses and a locally flat membrane. The optimal scenario for thrust and reflective purposes occurs when the membrane is loaded *uniformly* by applying equal radial forces: the central biaxial region has maximal area, and the wrinkles are symmetrically distributed around the membrane but confined to the vertices, see Fig. 1(b). For a triangular membrane, the wrinkles can still occupy as much as 20% of the total area (Stamper et al., 2000), but this reduces when the number of sides is increased. In practice, this demands extra cables and connections which add mass and complexity, and the optimal number of sides is governed by a trade-off analysis when other spacecraft performance metrics are considered.

Vertex wrinkling is unwelcome but it is not detrimental to the overall performance. However, if a cable fails, the applied loading must redistribute in a non-uniform way, and this can lead to asymmetrical load paths and the possibility of wrinkling across the membrane, even membrane collapse. Robust control of the displacement field with sensing, feedback and embedded actuation offers a potential solution but is challenging and beyond the scope

---

* Corresponding author. Tel.: +44 1223 764137.
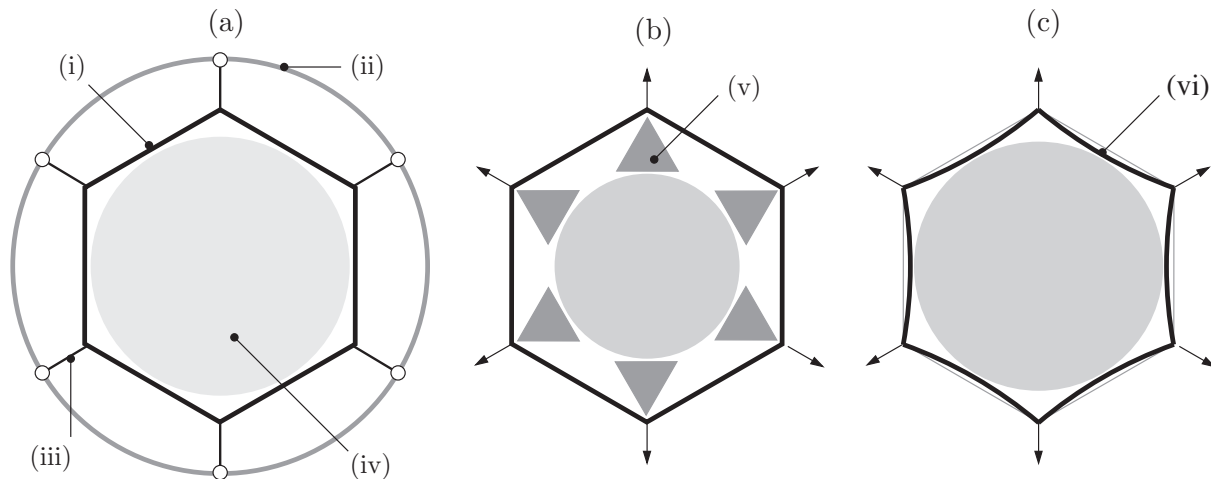 E-mail address: kas14@cam.ac.uk (K.A. Seffen).

Fig. 1. (a) Schematic layout of a reflective membrane structure for use as space telescope, taken from Santer and Seffen (2009). The polygonal membrane, (i), shown here to be hexagonal, is connected to an edge structure, (ii), through tensioning cables, (iii), at its vertices. When the membrane is completely flat, the inscribed circle, (iv), measures the largest useable optical area. (b) In practice, all corners of the membrane, (v), also schematic, are wrinkled orthogonally to the cable forces, thereby disrupting the flatness of the surface locally and reducing the useable area. (c) When the membrane edges are cut so that they form gentle curves initially compared to the straight edges, (vi), the wrinkles do not form under tensioning, and the useable area increases compared to (b).

of this paper: this is an active international research topic whose viability is mostly explored through computational simulations in which the actuating architecture and the effect of gravity can be more easily contrived; see Patterson and Pellegrino (2011) for a recent, seminal study. Mitigating wrinkles passively eliminates the need for a control system but is conceptually more difficult to achieve. One scheme uses a curved polygonal membrane with integrated edge cables, or cords, tensioned by the same vertex forces. As shown for the case of a square solar sail in Mikulas and Adler (2003), this arrangement can yield equal biaxial stresses everywhere but only at a specific value of pre-tensioning force, dependent on the edge curvature, the cord material and cross-sectional area, as well as the membrane properties. Generally, this force level reduces as the curvature increases, but the latter also decreases the useable membrane area: the cords add extra mass and can result in a heavier spacecraft overall by up to 50% compared to one without cords despite its membrane wrinkling (Mikulas and Adler, 2003).

In this paper, we address curved edges for passive elimination of vertex wrinkles but without using heavier edge cords. We are inspired by the efforts in Mikulas and Adler (2003), which show that edge-curving dramatically alters the membranal stresses, but also by computational results reported in an earlier undergraduate dissertation (Cunliffe, 2003), where compressive stresses were nullified altogether in a triangular membrane by gently "trimming" its edges. In practice, the original straight edges of the membrane are cut into circular arcs of central amplitude somewhere between 1% and 3% of the side-length. In Cunliffe (2003), trimming simulations are performed for a right-angled, isosceles membrane behaving as a biaxially-loaded quarter panel in a solar sail and, by trial and error, it is found that compressive stresses mostly disappear when all edges are trimmed to an amplitude of 2%. There is no formal calculation of the amount of trimming needed—both in this study and elsewhere, for example in Wang et al. (2008) it is stated that membrane-trimming by aerospace specialists is regularly undertaken "from intuition" rather than from calculations. Nonetheless, the effective levels of trimming seem to be very small, giving equally small reductions in the planform area; and, as the short table shows at the end of this paper, the associated gain in the useable membrane area is larger, especially for the most common of triangular and square sails.

Trimming is therefore a modest manufacturing detail offering discernible gains in membrane efficiency without adding any mass, and is worthy of further consideration.

We first present practical evidence of wrinkle mitigation through trimming that, to our knowledge, has not been reported in the literature, and is carried out in the following section. We compare uniformly tensioned membranes of the same size by starting with a straight-edged planform and examining its wrinkles as more edge-trimming is employed. Crucially, we observe that wrinkles disappear when the trimming amplitude is only a few percent, as suggested in Cunliffe (2003). We assess wrinkling by measuring the out-of-plane displacements using a 3D laser camera for both triangular and square membranes, where a complete displacement field yields information on the wrinkling distribution, and localised measurements offer detailed properties on the amplitude and wavelength of wrinkles. We confirm these findings in Section 3 using finite element analysis in two ways. First, we perform a linear membrane analysis in which bifurcation modes, which lead to out-of-plane displacements, are not sought. We do not employ a strict wrinkling criterion at this stage, rather, we aim to convey quickly how the responsible compressive stresses diminish throughout for small amounts of edge-trimming. Second, we perform a non-linear analysis for the same loading conditions in which wrinkling displacements prevail. Because of the associated computational challenges, wrinkles do not disappear altogether but their extent is reduced significantly. Finally in Section 4, we develop an original analysis of the effect of trimming. We do not attempt to capture wrinkling, rather we solve for the condition at which compressive stresses are eliminated in the vertices, and thus, our analysis is linear and valid for all values of applied loading, including those beyond which wrinkling might be expected. We do not solve the in-plane problem directly; instead, we choose a plate-bending approach based on the *static-geometric* analogy because this affords a visual interpretation of compatible bending displacements commensurate to the actual membranal stresses, which are more difficult to visualise. This aids our understanding of why trimming works, and we derive the optimal trimming condition for a general polygon, which, unsurprisingly, matches our experimental findings. This allows us to give guidance to designers of lightweight spacecraft on how effective trimming can be. Our study then concludes.

2. Experiments

Fig. 2(a) shows in plan view a radially-loaded equilateral triangular membrane made of Kapton, serial DK191 (Kapton, 2008), of thickness 0.025 mm, Young's modulus 2500 MPa and Poisson ratio, 0.34. This, and other planform shapes are made with the same circumscribing diameter of 635 mm: we found this size to be a good compromise between being small enough to handle easily and not to suffer adversely from gravitational effects, and being large enough relative to its thickness so that elastic wrinkles develop. Each planform outline is accurately obtained by sandwiching an over-sized piece of Kapton between precision-cut aluminium sheets, which are then clamped together so that excess Kapton can be cut away on the outside to leave a stress-free edge. Each vertex must be locally thickened by means of short Kapton "tabs", in order to avoid local tearing—as advocated in Wong et al. (2003), and each tab is connected to a length of metal studding passing through a rigid end-plate mounted on a wooden base, see Fig. 2(b). An axial compression spring is held in place between the end-plate and a wing-nut wound onto the studding so that, by turning the nut manually, the studding moves away from the membrane and the spring compresses, thereby applying a radial tensile force in a displacement controlled fashion. By using commercially-available precision springs, the magnitude of force can be accurately correlated with the number of turns after calibration.

Corner wrinkles are clearly evident in Fig. 2(c) after loading. In order to measure the associated displacements, we use a laser camera manufactured by Vialux (2013) to capture the spatial coordinates of the deformed membrane. The camera is coupled to a projector, and both are mounted on a fixed support structure. After calibration, the camera records the reflections of images projected onto the membrane, and associated software renders the corresponding shape of the surface as a "point-cloud" of data. The apparatus requires a low-reflective surface, and the particular Kapton has a white side for this purpose. The camera manufacturer guarantees an overall level of accuracy of 0.01 mm, depending on the width of the image field.

The membrane is loaded uniformly and incrementally in steps of 1 N, and visible wrinkles first appear in one corner at a force of 50 N. At 70 N, another corner begins to wrinkle, whilst the third corner remains flat along with rest of the membrane up to final load of 78 N; above this, the membrane is liable to fail by tearing near a tab. Wrinkles do not appear simultaneously or symmetrically in all corners because each loading nut is turned in sequence within a given loading step: wrinkles can appear suddenly in one corner, and appear to grow at the expense of those in other corners until their vertex forces become large enough to initiate mode

jumping. Such behaviour is commonly reported in many wrinkling tests despite best efforts to apply the loading evenly. Similar observations in the wrinkling character are made when the experiment is repeated for the same membrane, with only small variations in the threshold at which wrinkles initiate. We also made and tested a square planform with the same circumscribing diameter as the triangle. This begins to wrinkle in one corner at 40 N, and then diagonally opposite in another corner in the load range, 45–50 N; no other wrinkles form up to maximum load of 62 N with the rest of the membrane remaining flat.

These loads are taken as reference values for the performance of trimmed membranes of the same size, made with the same circumscribing diameter. Each membrane is manufactured in the same way using precision-cut templates with uniformly curved edges of increasing amplitude, given as a percentage value relative to the original side-length: the number of membranes used and their trimmed properties are indicated in Table 1. For the triangle, there are no visible wrinkles at full load when the degree of trimming is 1.5%; in some tests with the same specimen, wrinkles do not form at 0.75% but this is not conclusive because sometimes they do form and other times they do not. For the square, wrinkles do not form when the edges are trimmed by 3% although in other tests, they disappear at 1.5%. A summary is provided in Table 1.

Further evidence is given in Fig. 3, which compares the transverse displacements obtained across a corner section (S–S in Fig. 6) at which the original out-of-plane displacements are highest. In the untrimmed case, the waveform is clearly periodic with maximum amplitude in the centre. Its wavelength is approximately 7–8 mm, which is similar to the theoretical prediction in Bonin (2011) using a modified version of the well-known analysis by Wong et al. (2003). In the trimmed case, the membrane undulates close to the flat over most of its width with no distinctive waveform or periodicity to correlate with the presence of wrinkles. There is a narrow boundary layer on both edges where the maximum displacement is of the order of the original wrinkle amplitude: a possible explanation for this is given in the following section. At other locations along the vertex and at other vertices, trimming also reduces the periodicity and amplitude of wrinkles, and is repeated for the square membrane; the associated data are reported comprehensively in Bonin (2011).

3. Finite element analysis

We choose the commercially available software package, SAMCEF, developed by SAMTECH and the European Space Agency for bespoke analysis of membrane structures (SAMTECH, 2006). Out-of-plane capabilities are built into the suite of available elements,
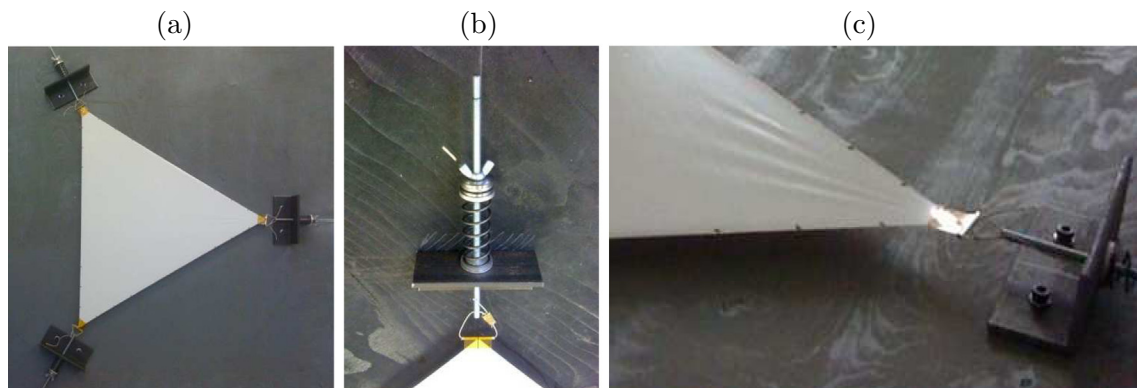
| (a) | (b) | (c) |

Fig. 2. Experimental set-up for assessing wrinkles in a triangular Kapton membrane of thickness 0.025 mm and edge length 55 cm. (a) Plan view of the membrane, tensioning elements and the wooden mounting plate. (b) Tensioning element detail. The membrane vertex is connected by a tab to threaded metal studding, which locates a precision spring. Turning the wing-nut shortens the distance between itself and the tab, thereby compressing the spring and generating a tensile axial force on the vertex. (c) Close-up view of radial wrinkles after tensioning the membrane. Kapton has a Young's modulus of 2500 MPa and a Poisson ratio of 0.34.

and so wrinkling behaviour is possible. Our study consists of both linear and non-linear analysis. In the first, we consider how the principal stresses behave under increasing degrees of trimming;

Table 1
Comparison of the wrinkled corners in practice as the degree of edge-trimming is increased for uniformly loaded triangular and square membranes. The percentage of trimming measures the amplitude of cutting relative to the side-length of membrane.

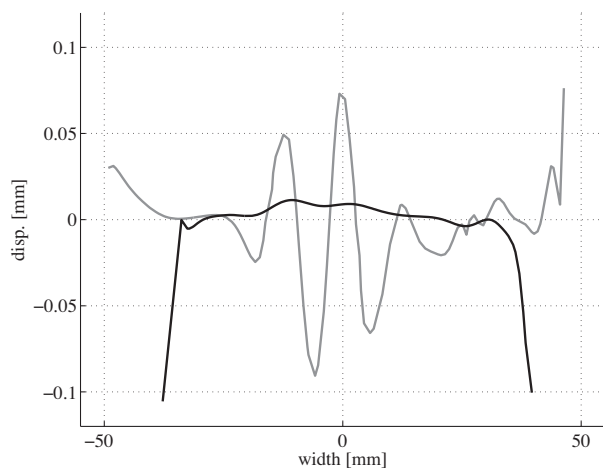| Planform	Edge-trimming (%)	No. wrinkled corners
Triangle	0	2
	0.75	0–1
	1.5	0
	3	0
Square	1.5	0–1
	3	0

Fig. 3. Out-of-plane displacements at one corner section of the tensioned membrane of Fig. 2 found by using a 3D laser camera. The section is located by S–S in Fig. 6, which is 10 cm away from the vertex. We are interested in the general variation; so the average displacement is set to be zero in both data sets. Grey: the membrane has straight edges and is wrinkled in the middle, where two large-amplitude waves are present. Black: the membrane edges have been trimmed to 1.5% amplitude, and the profile has no discernible wrinkles because the waveform is not periodic; but there are high displacements on both edges. In both, the original data are fitted with high-order polynomial curves for smoothness, and the camera is accurate to ±0.01 mm.

this analysis is relatively straightforward, and the characteristic form of stresses is independent of the load magnitude. There is also no need to include details of the reinforcing vertex tabs used in experiments as they only reduce the overall magnitudes of stress in practice, and all meshes are the simplest possible. In the second, we investigate the form of wrinkles by allowing out-of-plane displacements to develop throughout the membrane once buckling has taken place. This part is underpinned by a geometrically imperfect but stress-free mesh initially, in order to seed buckling, and this is described momentarily. Standard T053 triangular shell elements from SAMCEF's element library are used throughout because they have been developed specifically for non-linear wrinkling analysis. Each node has complete translational freedom, enabling out-of-plane displacements as well as in-plane strains, and rotations along the edges between elements are used to calculate bending moments within the membrane. Here, the magnitude of loading is important because of non-linearity, and the effect of the experimental vertex tabs is replicated by reinforcing the thickness fourfold in all corners over a triangular region with a base-width of 25 mm. This procedure is advocated in SAMCEF's technical guidelines for lowering stress concentrations and avoiding complications with forming very concentrated wrinkles adjacent to the corner node. In both the linear and non-linear cases, highly detailed meshes are needed to capture the rapidly varying stresses and displacements: in particular, at least eight elements per half-wavelength of wrinkle. For the present size and thickness of membranes, and following trial simulations, we settled on meshes with around 130,000 elements for the triangular case, and 160,000 for the square. As observed in experiments, the possibility of wrinkles forming asymmetrically on the membrane precludes the use of symmetry for reducing the mesh detail. The loading is applied as radially directed forces on each vertex node, with all other nodes unconstrained, and the material is specified to be linear elastic always, with the material properties corresponding to Kapton.

A typical set of principal stresses is given in Fig. 4. The first principal stresses are larger and positive and hence, tensile everywhere. They emanate radially from each vertex with contours of constant magnitude roughly similar to circular arcs. The contour density decreases towards the centre as the stress intensity decreases, and the shape of contours becomes less well defined. In the centre of the membrane, the stresses have no characteristic direction, but close to the edges, they are directed on gently curved, inward paths. The second principal stresses form circular and positive contours in the centre to comply with an equal biaxial stress state. In general they are smaller, and their magnitude
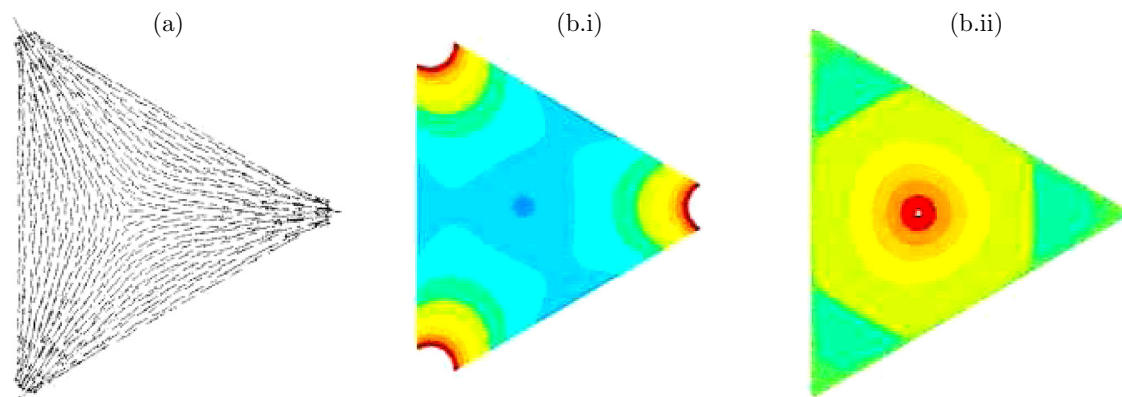

Fig. 4. Principal stress performance in a tensioned triangular membrane of the same geometry and material as Fig. 2. A linear finite element analysis is performed using the membrane analysis software, SAMCEF (SAMTECH, 2006). (a) Directions of the first (larger) principal stress shown as locally pointing arrows: they radiate along straight lines from each corner before curving round towards the middle. (b.i) Contours of first principal stress where the interest is in the shape of contours: the actual magnitudes do not matter. For an adequate separation of smaller stresses, the contours are not resolved in the corners, where the stresses are largest. (b.ii) Contours of second principal stress. At each corner, the magnitudes are negative, and in the centre, they are positive and equal biaxial.
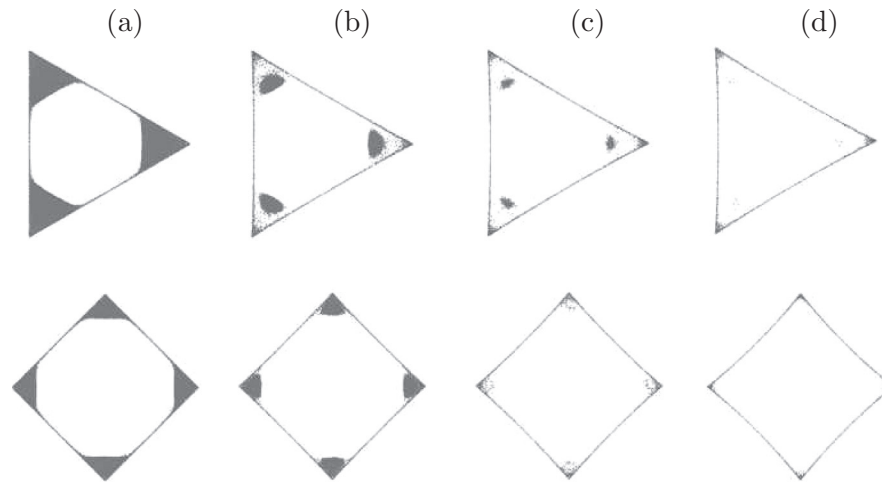
Fig. 5. Compressive stress performance of tensioned membranes with trimmed edges using a linear finite element analysis. The grey areas in the corners conform to negative second principal stresses without differentiating their magnitudes. Each column is for a specific amplitude of trimming, given as a percentage of the side-length of membrane: top; (a) 0%, (b) 1%, (c) 1.3%, (d) 1.5%: bottom (a) 0%, (b) 1%, (c) 2%, (d) 3%. In both triangular and square membranes, trimming clearly reduces the extent of compressive stresses; but more trimming is needed for a square membrane. For trimming levels beyond the maximum values quoted, there is no change in performance.
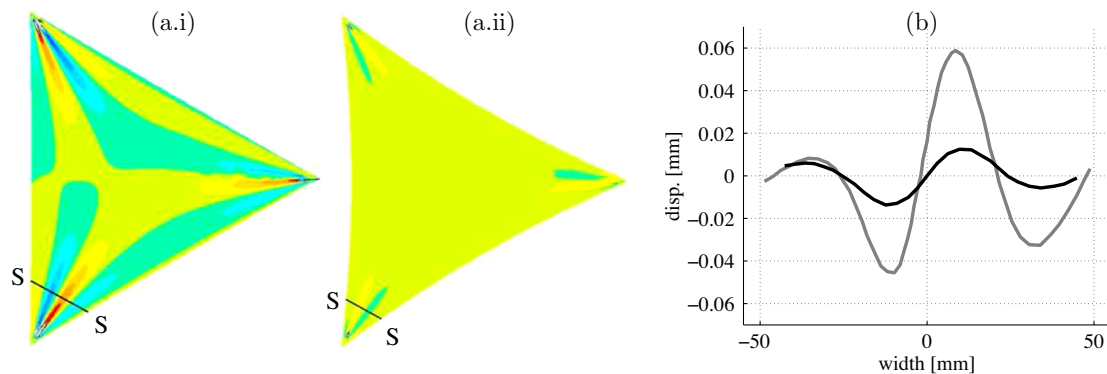

Fig. 6. Out-of-plane displacements in a tensioned membrane following a post-buckling, non-linear finite element analysis. The membrane has the same geometry and material as Fig. 2, and each vertex is locally thickened, as per experiment, over a side-length of 25 mm to prevent very high stresses. Different colours are different displacements, and the colour schemes match between sub-figures. (a.i) Straight-edged membrane with highly deformed corner regions, which modulate over the bulk of the membrane; (a.ii) the edges are trimmed to 3% amplitude, leading to both a more flat and less wrinkled membrane. (b) The cross-wise displacements in both at section S–S, where the displacement is maximal in the untrimmed case: grey refers to the untrimmed case, black is the trimmed case. The maximum peak-to-peak amplitudes compare well to Fig. 3.

reduces moving outwards into each corner, where they become compressive, *i.e.* negative over a sizeable region. Their direction is orthogonal to the first set, in the direction of out-of-plane buckling.

These compressive regions are isolated schematically in Fig. 5 for triangular and square membranes with trimmed edges. Each mesh is initially redefined with gently curved edges matching experiments and, as this increases, the compressive stresses naturally disperse. In the triangular case, the compressive regions shrink on all sides at 1% trimming; they persist in part at 1.3%, and are virtually eradicated at 1.5%—and all larger values. Similar features occur in the square case but at larger values of trimming; and, importantly, for both, the apparent elimination thresholds match experimental values from Table 1, which is encouraging. Although difficult to see, there are very narrow bands of compression running along all edges, which taper rapidly to zero on the free edge: this is a small boundary layer, which may be responsible for the rapidly changing edge displacements observed in practice in Fig. 3.

In the non-linear analysis, the possibility of wrinkling arises only if the mesh is imperfect in some sense: otherwise, it remains flat under loading but in a highly unstable manner. A geometrical imperfection is commonly achieved by superposing the out-of-plane displacement eigenmodes onto the original flat mesh, following a standard linear buckling analysis. We select the first four out-of-plane buckling modes for a mesh under tension, and normalise their displacements by setting the maximum value equal to one quarter of the membrane thickness. This imperfect but stress-free mesh is then loaded incrementally by vertex forces, and the system of equilibrium equations is solved in the current displaced configuration. During each loading increment, a dynamic analysis is employed as standard to impart numerical damping until a stable configuration is found, and the degree damping is systematically reduced until quasi-static conditions persist. This procedure is repeated for increasingly trimmed membranes, but we only focus on triangular membranes because they have the most extensive wrinkling.

Fig. 6 indicates the displacement fields at vertex forces of 78 N for 0% and 3% trimming: 3% is higher than the experimental threshold for wrinkling mitigation, yet wrinkles are still present. They extend around one-sixth of a side-length from each vertex, but the membrane is flat everywhere else: in the untrimmed case,
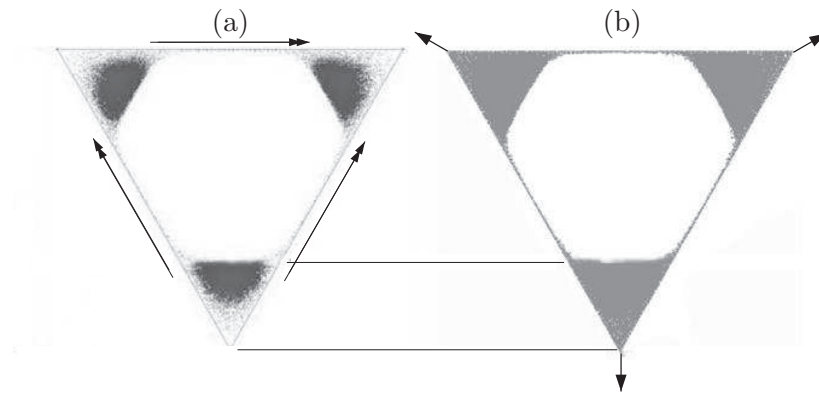
Fig. 7. Linear finite element analysis of (a) out-of-plane, plate-bending by virtue of equal edge rotations and (b) in-plane, uniformly tensioned membrane under vertex forces. The shaded regions indicate where (a) the second principal curvature in the radial direction and (b) the second principal stress orthogonal to radial lines are both negative, in order to highlight the effectiveness of the plate-bending analogy: horizontal construction lines between the bottom vertices show that both regions have virtually identical sizes.
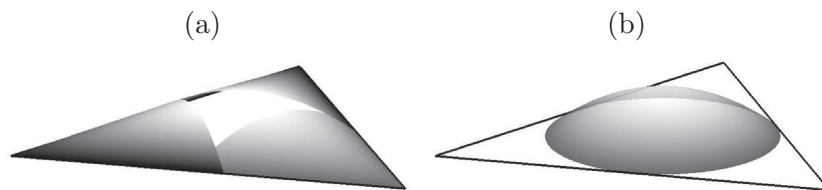

Fig. 8. Regional, elastic deformation modes in an originally flat plate undergoing edge-wise rotations. (a) Close to each corner, the rotations of adjacent edges dominate the response, giving rise to conical surfaces. (b) In the centre, the plate is equally curved in all directions to form a spherical cap. These modes are used to explain by analogy the stress performance in a tensioned membrane.
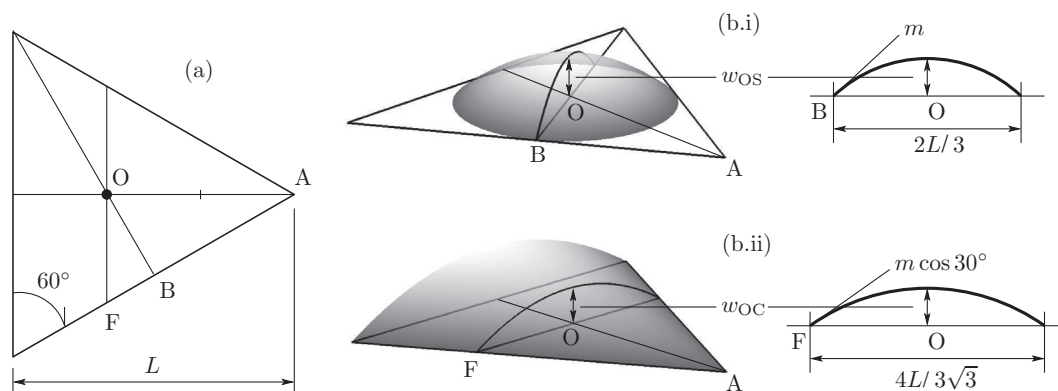

Fig. 9. The precise shapes of the deformation modes in Fig. 8 under edge-wise rotations, m. (a) Planform description of the triangular plate, identifying one vertex, A, and sectional points on the edge, B and F; the width of plate is L. (b.i) Cap deformation along the original line BO in (a). This is a shallow parabola with half-span, $L/3$, end-slope, m, normal to the edge, AB, and a final apex height above O, w_{OS}. (b.ii) Conical displacement field along FO: the half-span is $2L/\sqrt{3}$, the end rotation normal to FO is $m\cos 30°$, and the corresponding apex height is w_{OC}. The conical surfaces in other corners behave identically but are not shown for clarity.

the extent is about one-third, and the rest of the membrane is not flat: rather, it undulates gently in-and-out of plane. Wrinkles do not disappear altogether in the trimmed case because the initial imperfections must be large enough to ensure a wrinkling outcome and a convergent solution; if they are too small, wrinkling may never occur, and the effect of trimming remains undetermined. Inevitably, wrinkles are more extensively formed using this computational scheme, so in Fig. 6, the displacement profile remains wrinkled even though its counterpart in Fig. 3 does not, and the two profiles cannot be compared. However, it is reasonable to compare the displacement profiles within Fig. 6, which confirms a reduction in the maximum amplitudes and hence, some effectiveness in trimming.

4. Analysis

Up to the point of wrinkling, the ordinary membrane deforms entirely in-plane and is governed by plane stress elasticity for which the associated stresses can be studied using an Airy stress function, Φ (Timonshenko and Goodier, 1970). A trimmed membrane is similarly governed but we assume the amount of trimming is just enough to prevent wrinkling. Strain compatibility must be satisfied everywhere within the membrane, and is achieved by exactly solving $\nabla^4\Phi = 0$, where ∇^2 is the well-known Laplacian operator. The particular case of Flamant's solution for a tip-loaded wedge is analogous to a loaded vertex and is employed in many studies even though it does not account for the influence

of loads applied to the other vertices. Because of St Venant's principle, we may expect that this does affect the behaviour over a short radial distance away from the corner where, crucially, stress concentrations are highest in practice, and the results are typically robust. The stresses in the bulk of the membrane are not amenable in closed form by this route although there has been some success by approximating the membrane as a circular disk and superposing Flamant solutions, for example, see Bonin (2011). Calculating the stresses in a trimmed membrane is more challenging by definition because its curved edges are not immediately compatible with the polar coordinate system imbued within the Flamant-based approach. Furthermore, the effect of trimming appears to be disproportionate—where compression is mitigated outright by very small amounts of trimming. We either solve the original governing equation of compatibility for the actual trimmed geometry using a different Airy stress function, or we seek a different, approximate approach, as follows.

A cartesian (x,y) coordinate system specifies the planform geometry of the membrane. Since its edges are free of tractions, with the only external forces applied to the vertices, Φ outside of the membrane must be a linear function for compliance with this boundary condition; it may be locally zero on each edge but its gradient cannot be zero, otherwise the membrane inside is unstressed. Alternatively, we may think of Φ outside as separate planes on each side of the membrane, intersecting each edge so that $\Phi = 0$, with gradient, m, normal to each edge. Studying the function Φ becomes more amenable by noting that the deformation of a uniform elastic plate without normal loading must satisfy $\nabla^4 w = 0$, where w are small transverse displacements normal to the (x,y) plane. The benefits of a geometrical interpretation of stresses by analogy—the so-called "static-geometric analogy"—were originally set out in Calladine (1977), and the functions w and Φ are now equivalent under the same geometry and boundary conditions. This obviates setting $w = 0$ and its gradient equal to m on all edges, which is tantamount to the plate resting on simple supports before rotating about its edges by m by some arrangement of externally applied moments. The principal curvatures that emerge are now analogous to the principal stresses in the loaded membrane, but reciprocally so in terms of directions: if the x and y are orthogonal coordinates, the stress, σ_x, equal to $-\partial^2\Phi/\partial y^2$ by definition, correlates to the curvature, κ_y, equal to $\partial^2 w/\partial y^2$, and vice versa for σ_y and κ_x. By considering the displaced shape of plate and the corresponding principal curvatures, we may infer the stress performance of the membrane provided our approximation of the displacement field is robust, and this is performed shortly.

The effectiveness of the analogy is quickly evinced in Fig. 7, which compares the responses of a uniformly loaded triangular membrane of identical size and layout to a triangular plate bending transversely under rotations applied equally about all simply-supported edges. A linear finite element analysis is performed for both cases, and the familiar regions of membranal compression are highlighted, as they are in Fig. 5. We also highlight regions in the plate where the second principal curvature is found to be negative, and it is clear that their pervasion and distribution over the plate are virtually identical to the membrane.

In the following, we first consider the triangular case in detail because the manner in which its displacement fields satisfy compatibility are the simplest to visualise. We then show that trimming the edges but maintaining the boundary conditions allows these fields to be compatible without negative curvatures, thereby eliminating membranal compression by analogy; the required amount of trimming is determined as a closed-form expression. We then sketch the arrangements for a general polygon with inevitable repetition of the triangular case, but necessarily so for the sake of completeness. We then compare trimming predictions

to experiments involving the triangular and square plates, and elucidate trends for polygons with more sides.

4.1. Triangular membrane/plate

We may think of the displaced shape of a triangular plate under edge-wise rotations as having distinct but approximate regional forms, similar to the approach in Griffith and Taylor (1917) on the shape of soap films in torsion problems. Each vertex is clearly dominated by the rotations on adjacent edges and must adopt a shallow conical form, which rests on the original straight edges at angle, m, relative to the horizontal, see Fig. 8(a). These are singly curved across the straight radial generators, and this curvature is deemed positive for an upwardly displaced plate. In the centre of the plate, the edge rotations all contribute to the deformation isotropically, so the plate must form a shallow cap of equal principal curvatures, Fig. 8(b).

These displacement fields must also comply with the boundary conditions in the following way. The planform geometry of the plate is described in Fig. 9(a), which identifies the centroid, O, a vertex A, and points, F and B, on one edge where the conical and spherical regions respectively touch. The width of the plate is taken to be L, as shown. The normal displacements at O due to each surface are found from Fig. 9(b) by assuming that flat lines in the membrane deflect into shallow parabolas. For a general width of parabola, $2a$, with end slope, m', the apex height above the end points can be shown to be $m'a/2$. Thus, in the spherical region, the half-width, BO, is $L/3$ and w_{OS} is

$$w_{OS} = \frac{mL}{6} \tag{1}$$

where the second subscript denotes "spherical". On the other hand, the parabolic line on the conical surface meets the edge at 30° with a normal gradient in this direction equal to $m\cos 30°$. The half-width, OF, is $2L/3\sqrt{3}$, and

$$w_{OC} = \frac{1}{2} \times m\cos 30° \times \frac{2L}{3\sqrt{3}} = \frac{mL}{6} \tag{2}$$

which is the same as w_{OS}. The corresponding displaced shapes are now plotted in Fig. 10(a.i), and the region where they overlap is highlighted in terms of the disparity between displacements. In practice, the true extent of both surfaces is such that there is no disparity, but a side-view of the bisector in Fig. 10(a.ii) confirms that this is not possible if a conical generator remains straight. We are confident about the conical shape near the vertex but it must curve upwards closer to cap for continuity between the displacement fields. The precise description of the transition region between shapes does not matter, rather we see that straight generators cannot be straight locally but must have negative curvature, which suggests that the analogous principal stress is compressive in an orthogonal direction.

Fig. 10(b) indicates the conical and cap surfaces for a plate with trimmed edges. Each edge rotates about its end points by angle, m, and remains within the plane of rotation. The displacement fields are altered slightly but favourably so by reducing how much the surfaces diverge in the overlap region. Consider in plan view one edge of the original plate cut to a gentle parabolic shape with amplitude, δ, Fig. 11(a). After displacing upwards, the new apex height of the cap, w'_{OS}, is due to the cross-section in Fig. 11(b) having a full slope, m, over the outer part of width δ, and the usual parabolic shape of cap up to the apex over a reduced half-width, $L/3 - \delta$. Assuming small gradients and neglecting any intrinsic length changes, we have

$$w'_{OS} = m\delta + \frac{1}{2}m\left(\frac{L}{3} - \delta\right) = \frac{mL}{6}\left(1 + \frac{3\delta}{L}\right) \tag{3}$$

So, by having a fraction, $\delta/(L/3)$, of the half-span at full slope m, we increase w_{OS} by the multiplier, $(1 + 3\delta/L)$.

For the conical part, the effect of the boundary condition is rather more subtle. Original radial lines must remain straight after deformation, so the extent of the conical surface in a direction orthogonal to generators is limited by lines tangential to the curved edges where they meet at a vertex; on the outside of these lines, the plate can only deform at full slope, m. Over the centroidal position, recall that the conical half-span is $2L/3\sqrt{3}$, and, from Fig. 11(a), the width at full slope is shown to be $16\delta/3\sqrt{3}$. The fraction at full slope is therefore $8\delta/L$, and the new apex height is the previous value times this new multiplier, i.e.

$$w'_{OC} = \frac{mL}{6}\left[1 + \frac{8\delta}{L}\right] \tag{4}$$

Depending on the value of δ, the apex heights can be controlled relative to one another such that the previous necessity for a true, upwardly curving portion in the conical region can be avoided. One satisfying condition is that the radial bisector on the conical surface just touches the cap, as indicated in Fig. 11(c), where the full-slope portion at cap base is not included for simplicity because its effect on this position is negligible. The corresponding horizontal distance from the vertex can be verified as $\sqrt{3}L/2$, as shown, and in this view, the ratio of the apex eights can be found to be:

$$\frac{w'_{OC}}{w'_{OS}} = 8 - 4\sqrt{3} \Rightarrow \frac{1 + 8\delta/L}{1 + 3\delta/L} = 8 - 4\sqrt{3} \tag{5}$$

which returns $\delta/L = 0.015$. In experiments, the degree of trimming was normalised by the sidelength of triangle, denoted as l, equal to $2L/\sqrt{3}$, so $\delta/l = 1.3\%$. This is very close to the observed value of 1.5% for wrinkle mitigation in both experiments and in computation.

4.2. Polygonal membrane/plate

The planform geometry of a regular polygonal plate of n sides is given in Fig. 12(a), where the side-length is l and the vertex semi-angle is α. Again, we assume that the plate deforms under equal edge rotations, m, and that the displacement fields consist of identical conical regions near each vertex and a central cap whose limit of extent is the inscribed circle shown in Fig. 12(a). The corresponding apex height in the centre of the plate is found as before by assuming a parabolic cross-section over a half-span:

$$w_{OS} = \frac{m}{2} \times BO = \frac{ml\tan\alpha}{4} \tag{6}$$

where BO is the planform radius from a bisecting point, B, on one side to O, equal to $l\tan\alpha/2$. For each conical region, the shape is also defined by span-wise parabolas wrought under normal components of edge rotation, $m\cos\alpha$. These displacements do not match the cap shape moving towards the centre, rather, for continuity, the conical generators must curve upwardly, as per the triangular case. This feature is straightforward to verify and, analogously, is the source of compression and wrinkling in the original membrane. For the correct amount of edge-trimming, we postulate that the displacement fields are altered such that the radial bisector of each cone remains straight and tangential to the cap in one place. The scenario is highlighted in Fig. 12(b), which defines a horizontal coordinate, η, moving from the vertex, A, towards O.

The cross-section of the new cap has apex height, w'_{OS}, and the parabolic outline, w'_S, varies as

$$w'_S = \frac{w'_{OS}}{BO^2}\left[BO^2 - (AO - \eta)^2\right] \tag{7}$$

where, recall, BO is the planform radius. Again, the intersection point with the cone differs negligibly if the parabolic shape incorporates the effect of trimming—which we ignore at this stage. The conical bisector has displacement, w'_C, and is expressed by the linear height above O, w'_{OC}, as follows

$$w'_C = \frac{w'_{OC}}{AO}\eta \tag{8}$$

In practice, the conical region extends as far as a point P before O, where it glances the cap and $w'_{PC} = w'_{PS}$. This is a quadratic equation with a single root $\eta = \eta_P$, which is found by, first, defining $\rho = w'_{OC}/w'_{OS}$ and then setting the discriminant equal to zero

$$\rho^2\frac{BO^2}{AO^2} - 4\rho + 4 = 0 \Rightarrow \rho = 2\frac{AO^2}{BO^2}\left[1 \pm \left(1 - \frac{BO^2}{AO^2}\right)^{0.5}\right] \tag{9}$$

Substituting into the corresponding root expression

$$\eta = \eta_P = AE\left[1 - \frac{\rho}{2}\frac{BO^2}{AO^2}\right] \tag{10}$$

along with BO and AO equal to $(l/(2\cos\alpha))$ reveals that $\eta_P = l/2$. Rather neatly, this result is independent of the number of sides and α but we note that for $n \leqslant 6$, P is located before the point E, defined to be the limiting position on AO at which the conical cross-section is simply defined, Fig. 12(c): for $n > 6$, P lies beyond E, and the cross-sectional shape is not straightforward. As a
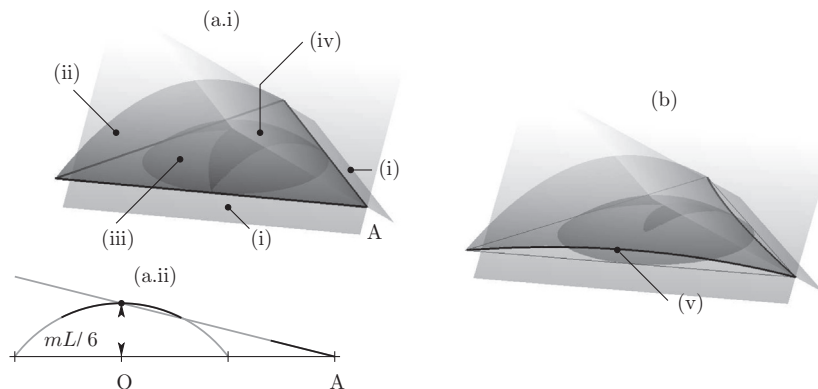

Fig. 10. Overlapping displacement fields from Fig. 9, considering one conical surface at A and the cap. (a.i) The edge-wise rotations, m, are shown as planes, (i), rotated about adjacent edges: the conical field is (ii) and the spherical region is (iii). The shaded region (iv) identifies that part of the conical field which lies below the spherical part, which is shown in (a.ii) for a radial bisector from A. Here, the displacements in the middle, $mL/6$, are calculated from the parabolic approximations in Fig. 9. (b) The original plate edges are now trimmed into gentle arcs, (v), and must remain within the rotation planes after deformation. The corresponding cone and cap displacements adjust, resulting in a smaller mismatched region near the centre.
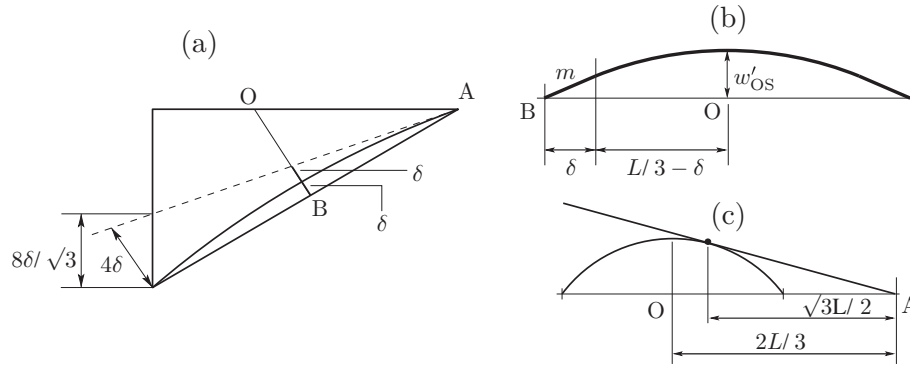
Fig. 11. Geometrical definitions for a deformed triangular plate with trimmed edges. (a) Planform view of half of the plate, where the amplitude of trimming is δ with respect to the original mid-point B. The dashed line is tangential to the curve at vertex A, which is separated from the tangent by 4δ at the rear face, with a transverse width $4\delta/\cos 30°$. (b) Elevation view of the displaced section of the original central cap, with new apex height, w'_{OS}. Over a width, δ, from B, the section must have a linear slope to conform with the rotated edge plane from Fig. 10. Over the remaining half-span, the section adopts the usual parabolic form. (c) Side-view of the radial bisector for identifying the point at which the conical generator touches the cap. Assuming the latter is parabolic, this distance is $\sqrt{3}L/2$ from A for a plate width of L.
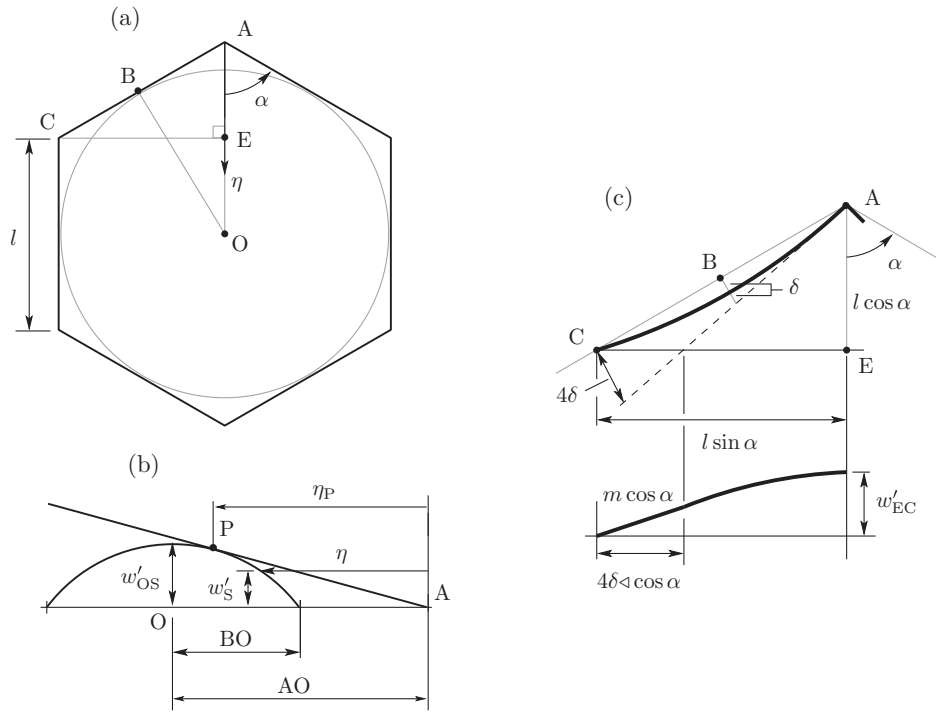

Fig. 12. Geometrical definitions for bending of a plate of polygonal outline, shown here as hexagonal: the vertex semi-angle is α, the side-length is l, and η is a coordinate with origin at the vertex, A. The mid-point of side AC is B, O is plate centre, and CE is normal to AO. (b) Side-view of the radial bisector showing a conical generator, AP, touching the spherical cap of radius BO. A general height is w'_S with respect to η, with an apex value of w'_{OS}. (c) Top: plan-view of a trimmed edge with amplitude, δ, at B. The normal width to the tangent at C is 4δ c.f. Fig. 11(a). Bottom: elevation view of the displaced conical section above CE, with apex height, w'_{EC} at E. The section must be linear up to the dashed tangent line, top, over a width, $4\delta/\cos \alpha$, and the remainder is parabolic: the edge rotation normal to CE is $m\cos \alpha$.

compromise, the conical height at P, w'_{PC}, can be calculated from that at E because the bisector is well defined, and $w'_{PC} = w'_{EC} \times (AP/AE)$.

So consider the cross-section with half-span CE normal to AE in Fig. 12(c). Recall from the triangular case that the tangent line at the start of the curved edge determines the width over which a linear slope is observed. This width is $4\delta/\cos \alpha$, see Fig. 12(c), and since $CE = l\sin \alpha$, then

$$w'_{EC} = m\cos \alpha \cdot \frac{4\delta}{\cos \alpha} + \frac{m\cos \alpha}{2}\left[l\sin \alpha - \frac{4\delta}{\cos \alpha}\right]$$

$$= \frac{ml\sin \alpha \cos \alpha}{2}\left[1 + \frac{4\delta}{l\sin \alpha \cos \alpha}\right] \tag{11}$$

and $w'_{PC} = w'_{EC}/(2\cos \alpha)$. The height of the cap at P, w'_{PS}, is found after replacing η with η_P in Eq. (7) and rearranging:

$$w'_{PS} = \frac{2w'_{OS}}{\tan^2 \alpha}\left[\frac{1}{\cos \alpha} - 1\right] \tag{12}$$

The new apex height is calculated from the original, Eq. (1), by noting that the fractional width of the amplitude of the trimmed edge is δ/BO, see Fig. 12, returning the following multiplier on w_{OS}:

$$w'_{OS} = w_{OS} \times \left(1 + \frac{\delta}{BO}\right) = \frac{ml\tan \alpha}{4}\left[1 + \frac{2\delta}{l\tan \alpha}\right] \tag{13}$$
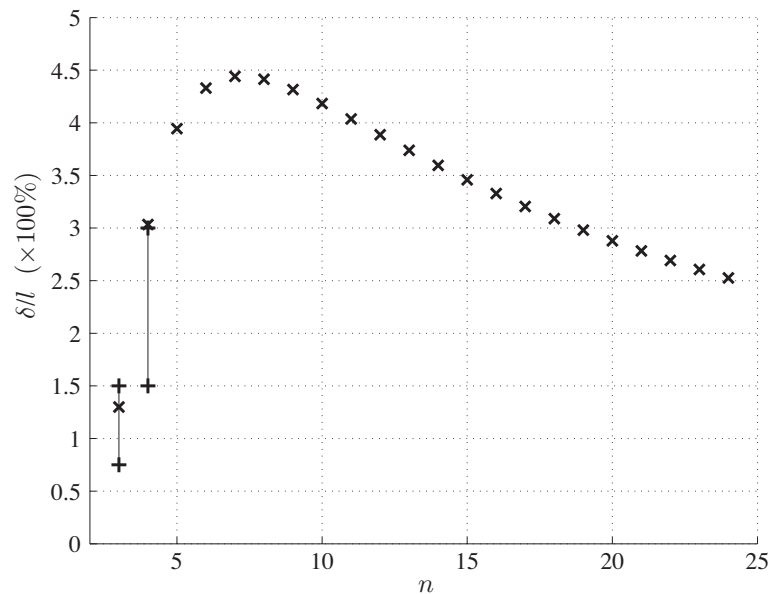
Fig. 13. Prediction by Eq. (14) of the required amount of edge-trimming for wrinkle prevention in a regular polygonal membrane of n sides. The side-length is l and the amplitude of trimming is δ: theoretical predictions ($\times$) are shown over a much larger range compared to experimental measurements ($+$), Table 1, on triangular and square outlines only. The latter are indicated as upper and lower bounds at which trimming was completely effective and sometimes effective, respectively.

Replacing w'_{OS} in Eq. (12) with Eq. (13) and equating w'_{PS} to w'_{PC} furnishes a unique solution for δ. After some manipulation, the final compact result is written as

$$\frac{\delta}{l} = \frac{1 - \cos\alpha}{4} \cdot \frac{\sin\alpha\cos\alpha}{\sin^2\alpha + \cos\alpha} \qquad (14)$$

The variation with the number of sides, n, is presented in Fig. 13 after converting α into the number of sides using the standard result, $(\pi/2)(1 - 2/n)$. Also plotted are the bounds from the experiments, Table 1, where the upper bounds match the predictions exceedingly well. The largest relative amplitude occurs for a heptagonal membrane, with $\delta/l = 4.5\%$, and the amount of trimming decreases as n increases beyond seven sides. In the limit, δ/l tends to zero as n becomes very large but this is not shown: an infinite number of sides conforms to a circular membrane, supported continuously on its circumference, which, recall, is biaxially stressed everywhere: it is not prone to wrinkling and no trimming is needed. A final point concerns the operational benefit of the membrane as a reflective surface. We previously defined an inscribed circle, Fig. 1, as the useful optical area, but we can simply measure the reduction in the total available area after trimming and compare this with the loss in area when wrinkling prevails without trimming. The results are given in Table 2 where the latter has been taken directly from a numerical study in Bonin (2011) by the first author: the benefits of trimming are clear.

Table 2
Comparison of the areas lost in a tensioned polygonal membrane of n sides. The trimming loss refers to how much of the original membrane needs to be physically removed at manufacture according to the prediction by Eq. (14): this assumes the remaining membrane area is completely flat after loading. The wrinkling loss refers to the area over which wrinkles prevail in the original membrane, thereby disrupting its flatness: these latter results are taken directly from Bonin (2011) following numerical calculation of the extent of the wrinkled region.

n	Trimming loss (%)	Wrinkling loss (%)
3	6.0	45.0
4	8.0	39.8
6	6.6	30.6
12	2.8	17.8

5. Discussion and conclusions

We have shown that trimming the edges of triangular and square membranes into gentle circular arcs of amplitudes 1.5% and 3%, respectively, can dramatically reduce the extent of corner wrinkles that tend to arise naturally when the membrane is uniformly tensioned by discrete vertex forces. We have given an overview of the empirical evidence from physical experiments and finite element analysis. The former are carefully arranged, small-scale tests using Kapton, a space-qualified material often used in the design of Gossamer structures, and the wrinkling characteristics have been quantified visually by inspection and by measurement using a laser camera. Computational analysis has enabled us to more fully understand the development of compressive stresses responsible for wrinkling, and we have focussed mainly on determining how extensive the wrinkle profiles are rather than calculating the stress limits at which wrinkling begins: in doing so, our scheme for preventing wrinkles adopts a geometrical perspective instead of managing loads, and this may simplify the design of full-scale structures as well as improving their robustness in operation because we have focussed on geometry. We have also furnished a qualitative treatment of how trimming affects the distribution of compressive stresses, but we have solved the analogous problem of a uniform plate, of identical planform, rotating about simply-supported edges, where the presence of negative principal curvatures correlates to membranal compression in practice. The optimal level of trimming predicted by this approximate model matches our experiments very well. Our structures are, however, small scale, when proposed Gossamer structures can be several orders of magnitude larger in size for similar levels of thickness; but, as noted, our analysis is linear and its predictions levels ought to be independent of scale. We hope that this may be confirmed by others in the future.

References

<www.vialux.de/HTML/en_ddscan.htm>, 2013, Vialux.

Bonin, A.S., 2011. Wrinkling in Polygonal Membranes (Ph.D. dissertation). University of Cambridge.

Calladine, C.R., 1977. The static-geometric analogy in the equations of thin-shell structures. Math. Proc. Camb. Philos. Soc. 82, 335–351.

Cunliffe, W., 2003. De-wrinkling of Membranes (MEng dissertation). University of Cambridge.

Griffith, A., Taylor, G.I., 1917. The use of soap films in solving torsion problems. Proc. Inst. Mech. Eng., 755–789.

Kapton, 2008. <www2.dupont.com/Kapton/en_US/assets/downloads/pdf/HN_datasheet.pdf>, Dupont.

Mikulas, M.M., Adler, A.L., 2003. Rapid structural assessment approach for square solar sails including edge support cords. In: Proceedings of 44th AIAA/ASME/ASCE/AHS/ASC Structures, Dynamics and Materials Conference, Norfolk, Virginia, USA, 2003, paper 2003-1447.

Patterson, K., Pellegrino, S., 2011. Shape correction of thin mirrors. In: Proceedings of 52nd AIAA/ASME/ASCE/AHS/ASC Structures, Dynamics and Materials Conference, Denver, Colorado, USA, 2011, paper 2011-1827.

SAMTECH, Projet PATISS, Dossier de Tests, Summary Report, 2006.

Santer, M.J., Seffen, K.A., 2009. Optical space telescope structures: the state of the art and future directions. Aeronaut. J. 113 (paper 3348).

Stamper, B., Angel, J.R.P., Burge, J.H., Woolf, N.J., 2000. Flat membrane mirrors for space telescopes. Proc. SPIE 4091, 126–136.

Timonshenko, S.P., Goodier, J.N., 1970. Theory of Elasticity. McGraw Hill, New York.

Wang, X., Sulik, C., Zheng, W., Hu, Y.R., Potvin, M.J., 2008. High fidelity wrinkling analysis of membrane structures and elliptical cut optimization. In: Proceedings of 49th AIAA/ASME/ASCE/AHS/ASC Structures, Dynamics and Materials Conference, Schaumberg, Illinois, USA, 2008, paper 2008-2255.

Wong, Y.W., Pellegrino, S., Park, K.C., 2003. Prediction of wrinkle amplitudes in square solar sails. In: Proceedings of 44th AIAA/ASME/ASCE/AHS/ASC Structures, Dynamics and Materials Conference, Norfolk, Virginia, USA, 2003, paper 2003-1982.